Acoustic Lagrangian velocity measurement in a turbulent air jet

Philippe Gervais, Christophe Baudet, Yves Gagne

Acoustic Lagrangian velocity measurement in a turbulent air jet

P. Gervais, C. Baudet, Y. Gagne

Abstract Measuring Lagrangian velocities in a turbulent flow is of a great interest for turbulence modeling. We report measurements made in an axisymmetric turbulent air jet at Reynolds number $R_\lambda \simeq 320$, using acoustical Doppler scattering. Helium-filled soap bubbles are used as Lagrangian tracers. We describe an experimental setup which allows the simultaneous measurement of the full three-component Lagrangian velocity and the longitudinal Eulerian one. Lagrangian velocity probability density functions (PDF) are found Gaussian, close to Eulerian ones. Velocity correlations are analysed as well as the statistical dependence between components.

1 Introduction

The most common way of measuring a quantity in a fluid is to set up a probe at a fixed point in space. This is the Eulerian point of view. A second way is to measure quantities along fluid particles trajectories, which is the Lagrangian point of view. Whereas Eulerian statistics are dominated by spatial features of the velocity field, Lagrangian one gives the temporal evolution along a fluid particle trajectory. Practically, the achievement of actual measurements of Lagrangian quantities is a real challenge. For this reason, turbulence has been studied experimentaly mainly from the Eulerian viewpoint. Thanks to recent technological and theoretical advances, Lagrangian studies of turbulence received a renewed interest.

Sato and Yamamoto (1987) measured simultaneously two velocity components of a single Lagrangian tracers in a grid turbulence flow. They extensively studied particle diffusion and velocity autocorrelation. The use of a video camera constrained the measurements to very low Reynolds numbers, for which turbulence cannot be considered to be fully developed. With several cameras, one can simultaneously get the three-dimensional trajectories for several particles. Ott and Mann (2000) studied three-dimensional diffusion of particle pairs in a flow with no mean velocity, and compared experimental results with theoretical models. Virant and Dracos (1997) made similar measurements in an open channel flow. Because of the relatively low frame rate of video cameras, studies were restricted to low Reynolds number flows ($R_\lambda < 100$) in laboratory experiments. Increasing the frame rate implies increasing the data rate, and technical limitations are quickly reached. One solution to this problem is to restrict the measurement to a single particle at a time. Its position can then be obtained with one-dimensional sensitive devices, reducing significantly the data rate, thus allowing to increase the sampling rate. This principle has been applied by Voth et al. (2002). They were able to fully resolve the Kolmogorov time scale, in a very high Reynolds number flow (Von Kármán swirling flow,

P. Gervais · C. Baudet · Y. Gagne
Laboratoire des écoulement géophysiques et industriels,
BP 53, 38041 Grenoble cedex 9, France

C. Baudet
e-mail: baudet@hmg.inpg.fr

Y. Gagne
e-mail: gagne@hmg.inpg.fr

Present Address:
P. Gervais (✉)
LEPTAB, av. Michel Crépeau,
17042 La Rochelle Cedex 01, France
e-mail: pgervais@univ-lr.fr

at $R_\lambda \geq 500$). Unfortunately, the volume where the measurements took place was so small that only acceleration could be studied, for which a very strong intermittency was observed.

All the above techniques give particle position along time. Velocity is obtained by numerical differentiation, which is a very noise-sensitive technique. Mordant et al. (2001) used Doppler frequency shift of acoustic waves scattered by tracer particles to obtain Lagrangian velocity in a Von Kármán flow. Since the frequency shift is proportional to the velocity, no differentiation operation is necessary to get the instantaneous velocity. Acoustic scattering imposed a minimal tracer size, which was larger than the Kolmogorov scale. It bounded the minimal measurable time scale by a few Kolmogorov time scales. The upper bound is given by tracers detection duration, which was several integral time scales long. They reported very strong intermittency: the probability density functions of velocity increments are Gaussian for large time separations and become increasingly non Gaussian as time separation get smaller. Velocity correlations were shown to be very close to an exponential shape, as expected theoretically (see Monin and Yaglom 1975 and references therein).

In neither of the previous studies a clean comparison between Lagrangian and Eulerian statistics in turbulent flows were made, either because Eulerian measurements were not available (Voth et al. 2002; Mordant et al. 2001), or because Reynolds number was too low, so that turbulence cannot be considered as fully developed (Virant and Dracos 1997; Ott and Mann 2000; Sato and Yamamoto 1987). In the present paper, we describe an experimental setup allowing to perform simultaneous Lagrangian and Eulerian measurements in a turbulent air jet ($R_\lambda \simeq 320$). Small helium-filled neutral soap bubbles are seeded from a position upstream from the nozzle. The three components of the Lagrangian velocity are obtained by acoustical Doppler effect. The detection setup, as well as the tracers are described in part 2. In part 3, we present the signal processing techniques used to detect the passage of bubbles and then to extract their velocities from the frequency shifts. In part 4, we report results on the main statistical properties of the velocity signals.

2 Experimental setup

2.1 Flow facility

All measurements have been conducted in a round air jet, emerging from a 2.25 cm conic nozzle (diameter d) and expanding freely in the room. The mean flow and the turbulence flow become self-similar at a distance of approximately 40 times the nozzle diameter, with a virtual origin $x_0 \simeq 4d$ (Wygnanski and Fiedler 1969). Measurements have been performed at four distances up to 110 diameters dowstream (Table 1).

In all experiments, the Reynolds number is held at a constant value, corresponding to a mean nozzle velocity around 43 m s^{-1}. For each downstream position, the hot-wire is located at the center of the acoustic scattering measurement volume. The hot-wire, home made with Wollaston wire, has a diameter of 3 μm, a sensitive length $l_s \simeq 300$ μm. It is operated with a constant temperature anemometer (CTA DISA 55M01). Electric signals delivered by the CTA, are digitized at a 65,536 Hz sampling frequency. Finally they are converted into flow velocity data using the usual King's law, which coefficients are determined by a previous calibration obtained with Pitot measurements. The overall cut-off frequency of the anemometry chain has been estimated to be larger than 20 kHz (for all downstream positions), by means of a square signal test procedure. From the longitudinal velocity data samples, measured on the jet axis, we have estimated some jet characteristics, based on the following classical isotropic relations and the Taylor frozen-turbulence hypothesis (Pope 2000; Tennekes and Lumley 1992):

- the turbulent streamwise velocity fluctuations $u^{\mathrm{E}}_{\mathrm{rms}}(x)$ (of order $0.25\langle U_{\mathrm{E}}\rangle(x)$, where $\langle U_{\mathrm{E}}\rangle(x)$ is the streamwise mean velocity) measured on the jet axis at a given location x;
- the mean dissipation rate of energy $\epsilon = -\frac{5}{4}\frac{S_3(l)}{l}$, where $S_3(l)$ is the third order velocity structure function and l a spatial increment in the inertial range;
- the Eulerian integral scale $L_{\mathrm{E}} = \langle U_{\mathrm{E}}\rangle \int_0^\infty C_{\mathrm{uu}}(\tau)d\tau$, with $C_{\mathrm{uu}}(\tau)$ the longitudinal velocity autocovariance function;
- the Taylor scale $\lambda = \left(\frac{15\nu}{\epsilon}\right)^{1/2} u^{\mathrm{E}}_{\mathrm{rms}}$;
- the Kolmogorov scale $\eta = \left(\frac{\nu^3}{\epsilon}\right)^{1/4}$.

Table 1 Statistical features of the Eulerian velocity (measured on the jet axis) at the four downstream distances x from the nozzle investigated in the present study

x (m)	$\langle U_{\mathrm{E}}\rangle$ (m/s)	ε (W/kg)	L_{E} (cm)	λ (cm)	η (mm)
1.3	4.85	21.3	6.2	0.44	0.12
1.8	3.45	5.34	8.8	0.62	0.17
2.1	2.90	2.80	10	0.73	0.20
2.5	2.45	1.35	12	0.88	0.24

2.2 Detection principle

The principle of a one-component velocity measurement is presented schematically in Fig. 1. A continuous ultrasonic sound wave of frequency 110 kHz ≤ ν ≤ 130 kHz, originating from an emitting transducer is directed towards the jet, along vector $\mathbf{n_i}$. Tracers (soap bubbles) following the flow scatter the wave. The sound wave, with frequency ν', scattered in a specific direction ($\mathbf{n_d}$) is recorded by a receiving transducer. Incident and scattered frequencies ν and ν' are related by the following relation (Doppler effect) :

$$\frac{\nu' - \nu}{\nu} = \frac{\mathbf{V}(\mathbf{n_i} - \mathbf{n_d})}{c} = -2\frac{V_{//}}{c}\sin(\theta/2) \qquad (1)$$

Extraction of the instantaneous scattered frequency thus gives the projection of the tracer velocity along the direction of the vector $\mathbf{n_i}$–$\mathbf{n_d}$. The sign of ν'–ν gives the trajectory orientation (downstream or upstream from the nozzle).

The electric signal originating from the receiver is digitized by a HP E1430A card at 65,536 Hz after digital heterodyne demodulation. Series of 1,048,576 samples are recorded. Within each series, several isolated bubbles are successively detected. Transducers are of capacitive type (reversible), working as emitter as well as receiver. Their surface is plane circular, with a diameter D_{Trans} = 24 cm. Thanks to the transducers high directivity, tracers can only be detected when they are located in the volume defined by the intersection of the incoming and detection transducer beams, which will be called in the following the ''acoustic measurement volume''. A schematic of the set-up is sketched in Fig. 1.

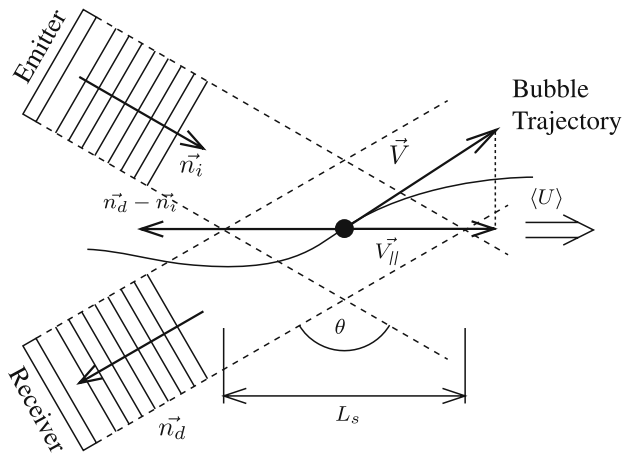

Fig. 1 Principle of the acoustic measurement of one projection of the advection velocity of tracers using one pair of transducers. Bubbles are only visible in the intersection of the two acoustic beams (*dashed lines*), defining the acoustic measurement volume ($L_s \simeq 50$ cm)

One challenge arising in Lagrangian measurements is to follow the tracers long enough. This means that we seek to record the velocity of a single tracer for a time T_s larger than the Lagrangian integral time scale T_L. A simple order of magnitude calculation gives hints about ways to achieve this experimentally. It was shown numerically (Yeung 2002) that the Eulerian time scale $T_E = L_E/u^E_{rms}$ is related to the Lagrangian time scale by $T_L = 0.78T_E$ (L_E is the Eulerian integral length scale and u^E_{rms} is the velocity standard deviation). The maximum time-of-flight in the measurement volume is $T_s \simeq L_s/\langle U_E \rangle$. In the turbulent free jet, the ratio $u^E_{rms}/\langle U_E \rangle$ on the jet axis is independent of both the longitudinal position and the Reynolds number. Therefore, $T_s/T_L \simeq (L_s/L_E)/3.12$. Maximising T_s/T_L is then only a matter of maximising L_s/L_E, which is completely independent of the velocity at the nozzle. With the chosen value for L_s, L_s/L_E ranges from 8 to 4, respectively for a measurement volume located 60 and 110 diameters downstream from the nozzle. The maximum value for T_s/T_L is then expected to be between 2.6 and 1.3.

2.3 Three-component measurements

By using more than one pair of transducers, simultaneous three-component measurements can be achieved. Four transducers (two emitters, two receivers) are placed at the vertices of a square, their axes crossing the same point on the jet axis, forming a square-based pyramid (Fig. 2). Distances from transducers to the intersection with the jet axis are all identical, ensuring that wave propagation delays are all identical. Transducers are reverse-facing the nozzle, to avoid bubble impacts on their active surfaces.

The first emitter E1 generates a continuous wave at frequency ν_1 = 110 kHz, scattered by each bubble, and then recorded in two different directions by the two receivers (R1 and R2, respectively). This gives access to two projections of the tracer velocity, respectively along vectors **j** and **l**. Similarly, the wave emitted by E2, at frequency ν_2 = 122 kHz (different from ν_1) is also scattered and then recorded by the two receivers, giving access to two more projections along vectors **k** and **i**. Provided the bubble lies in the intersection of the four acoustic beams, its velocity can be obtained through four non-orthogonal projections, which we will denote by (ν_i, ν_j, ν_k, ν_l). Components along and perpendicular to the jet axis (u, v, w) can then be computed by a simple matrix transformation.

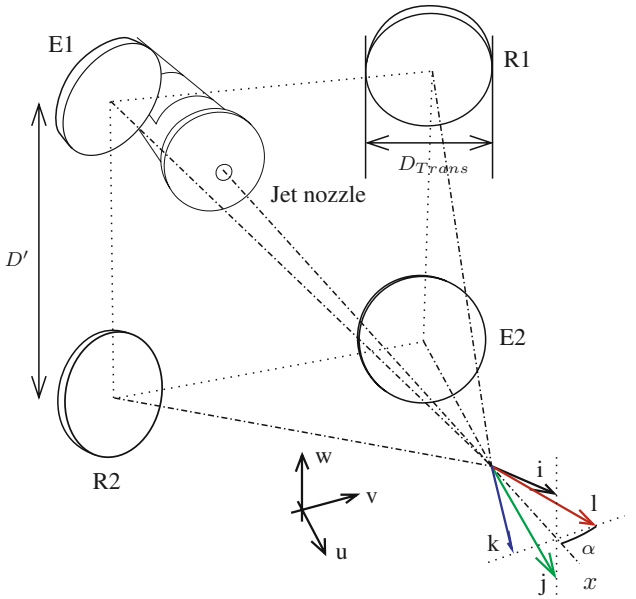

Fig. 2 Transducers arrangement for three-component measurement. D_{Trans} = 24 cm, $D' \simeq 50$ cm. Emitters are referred to as E1 and E2, receivers as R1 and R2. $\alpha = 26°$, yielding a scattering angle θ of 128° (see Fig. 1)

Beside the fact that this system gives access to the bubble velocity vector, it has several advantages over the simpler one-dimensional setup. These advantages all lead to improvement of the signal to noise ratio (SNR) of the recorded acoustic signals.

The first characteristic that increases the SNR is redundancy. The velocity components (u, v, w), can be simultaneously obtained from the v_i, v_j, v_k and v_l by the formulas (α is defined in Fig. 2):

$$u = \frac{v_i + v_j + v_k + v_l}{4\cos\alpha}$$

$$v = \frac{v_l - v_k}{2\sin\alpha} \qquad w = \frac{v_i - v_j}{2\sin\alpha}. \tag{2}$$

We assume that each projection (v_i, v_j, v_k, v_l) is affected by an independant additive random noise of variance σ^2. Therefore, noise for u has a variance of $\sigma^2/4\cos^2\alpha \simeq \sigma^2/3.23$. Noise variance for v and w is $\sigma^2/2\sin^2\alpha \simeq \sigma^2/0.38$. A real increase in SNR is obtained for the longitudinal component compared to the one-dimensional case. This is not true for transverse components due to less redundancy (the factor of 2 for transverse instead of 4 for longitudinal in Eq. 2).

With working frequencies in the 100–150 kHz range, acoustic absorption is far from being negligible. Sound paths have to be as short as possible. A second advantage of the pyramidal setup is that transducers separation distance D' can be made very short without perturbing the flow, because of the round shape of the jet. For a given scattering angle (which will be discussed below), acoustic path is then shorter for the three-component measurement setup than for the one-dimensional one.

Despite the transducers high directivity, some acoustic energy still propagates straight from each emitter to each receiver, responsible for a spurious signal at the emitting frequency. As the wave travels across the turbulent flow, it is phase- and amplitude-modulated (scintillation, Monin and Yaglom 1975). A final advantage of the pyramidal setup is that scintillation is greatly reduced. For reasons that will be discussed below (3.1), this increases the accessible velocity range and eases the signal processing.

2.4 Acoustic measurement volume and flow inhomogeneity

Ideally, the measurement volume is experimentally defined by the domain where four projections of the velocity vector can be obtained at the same time. Figure 3 shows a polygonal approximation of the whole measurement volume. In most cases, four projections are available for the computation of the three components of the velocity vector. Note that, however, in a restricted proportion of cases (estimated to be of order 17% from geometrical constructions), only three projections will be accessible, instead of four, corresponding to particles travelling close to the lateral boundaries of the main acoustic volume. In these latter situations, noise variance will increase up to $\sigma^2/1.62$ for

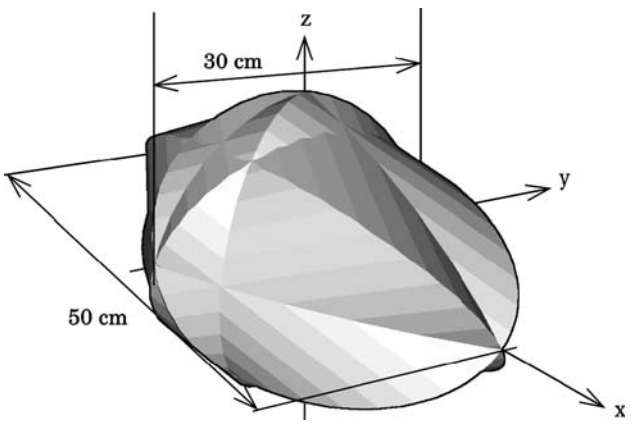

Fig. 3 Polygonal approximation of the acoustic measurement volume, defined as the domain wherein a bubble is visible from the four acoustic scattering channels allowing the determination of four independent projections of the instantaneous Lagrangian velocity vector

the longitudinal component and $\sigma^2/0.13$ for the transverse ones.

Jet flows are characterized by a strong spatial inhomogeneity, particularly in the transverse direction, manifested by the shape of the mean velocity profile. Thus, Lagrangian particle trajectories should be parameterized, at least by their initial position. As our measurement set-up does not provide any absolute particle position information, we adopt an alternate conditioning based on the duration of the particle trajectory in the acoustic volume. For each tracer particle entering the acoustic measurement volume, signals corresponding to three or four projections of the instantaneous velocity vector are collected during the time the particule is detected. Due to the limited extent of the acoustic measurement volume and to its elongated shape depicted in Fig. 3, the duration of the particle trajectories strongly depends on the initial position. The longest trajectories are expected to occur for particles travelling close to the jet axis where the longitudinal extension of the measurement volume is maximum. Our conditioning strategy consists in discarding all velocity segments with a total duration smaller than a prescribed threshold.

Thus, our measurements are affected by two kinds of spatial inhomogeneity. On the one hand, the transversal heterogeneity of the streamwise velocity component induces a lack of spatial homogeneity of the initial particle velocities when they enter the measurement volume. On the other hand, the decay of this mean velocity along the jet axis is responsible for a lack of temporal stationarity of each lagrangian velocity segment as the particle travels across the measurement volume in the downstream direction. With regard to the first problem (transverse spatial heterogeneity), there are two effects which accentuate (respectively lessen) the departure from homegeneity: the spatial dispersion of the particle positions entering the acoustic volume which continuously increases with the downstream location of the measurement volume and respectively the increasing relative extent of the transverse velocity profile with respect to the fixed lateral size of the acoustic measurement volume. A qualitative estimate of the transverse inhomogeneity is given by the ratio of the transverse half-size $R_{\mathrm{vol}} \simeq 15\ cm$ of the measurement volume (displayed in Fig. 3) to the radius $R(x)$ of the transverse profile of the streamwise velocity where $U(x,R) = 0.8\langle U_{\mathrm{E}}\rangle(x)$. Using the classical round jet mean velocity profile $U(x,r)/\langle U_{\mathrm{E}}\rangle(x) \sim \frac{1}{(1+a\eta^2)^2}$ (with $\eta = r/(x - x_0)$). The normalized value of 0.8 corresponds to $\eta = 0.05$ and leads to $R(x)$, respectively equals to 6, 8.6, 10 and 12 cm at $x = 1.3$, 1.8, 2.1, 2.5 m, respectively downstream from the nozzle.

Keeping in mind that most of particle trajectories remain roughly in straight line and close to the jet axis (particularly at the nearest downstream position $x = 1.3$ m), the comparison of these estimations with R_{vol} suggests that, whatever the distance x, the mean streamwise velocity of particles stays, on the whole, comparable to $\langle U_{\mathrm{E}}\rangle(x)$ within 20%. This qualitative comment will be confirmed by the experimental results presented below in sect. 4.3. As for the mean flow inhomogeneity related to the decaying of the mean velocity streamwise component downstream from the nozzle, it is possible, as suggested in Yeung (2002), to correct the bias resulting from the lack of temporal stationarity of the Lagrangian velocity signals. Yeung (2002) proposed to make each time series (each particle trajectory) covariance stationary by subtracting the appropriate local mean velocity and dividing by the local standard deviation. As such temporal non-stationarity effects are expected to strongly affect correlation estimates, we describe in more details in Sect. 4.3 the stationarization procedure, used in the present investigation.

2.5 Tracers

The problem of relating the tracer velocity to the true local fluid velocity has been fully adressed from the theoretical stand point by Maxey and Riley (1983), and recently from direct numerical simulations by Bec et al. (2006). First, material tracer particles are subjected to forces exerted by the surrounding fluid, in particular: the pressure gradient and the viscous shear stress (Stokes drag). The viscous drag is mainly responsible for a low pass filtering of the temporal response of the particle velocity to sudden changes in the forces exerted by the surrounding fluid flow. For spherical particles, the Stokes response time is given by $\tau_s = 2\rho_{\mathrm{p}}a_{\mathrm{p}}^2/(9\rho_{\mathrm{f}}\nu)$ (a_{p} is the particle radius, ρ_{p} and ρ_{f} the particle and fluid density, respectively, and ν is the kinematical viscosity). In the present experiment, the Stokes response time leads to values of the Stokes number $\mathrm{St} = \tau_{\mathrm{s}}/\tau_\eta$ ($\tau_\eta = (\nu/\varepsilon)^{1/2}$ is the Kolmogorov timescale) ranging between $\mathrm{St} = 4.4$ and 17.7, depending on the downstream position (Table 2). In view of the Stokes numbers of the tracer particles used in this experiment, significant reductions of the particle acceleration variance with respect to that of true fluid particles are expected and should be taken into account for, by a proper modelization of the filtering kernel, in further studies of statistical Lagrangian intermittency (out of the scope of the present investigation). According to the numerical study performed

Table 2 Estimations of the Stokes number and of the ratios of turbulent scales to particle radius at the four downstream distances x from the nozzle, investigated in the present study

x [m]	1.3 m	1.8 m	2.1 m	2.5 m
St	17.7	8.8	6.4	4.4
λ/a_p	4.4	6.2	7.3	8.8
η/a_p	0.12	0.17	0.20	0.24

by Bec et al. (2006), any density mismatch (influencing the estimation of the Stokes number through the ratio ρ_p/ρ_f) is also responsible for strong segregation effects induced by differential buoyancy: particles heavier than the suspending fluid tend to be expulsed from the regions with a high vorticity level and conversely for particles lighter than the fluid. As such preferential concentrations could result in a non uniform sampling of the flow field and, in turn, in strong statistical biases (Voth et al. 2002), a good density matching is desirable, independently of any Stokes number consideration. To reach a proper density matching, a main concern when looking for Lagrangian tracers in air flows, we used helium-filled soap bubbles. Bubbles are produced with the desired density by a dedicated machine, and injected just upstream from the nozzle, so as to limit disturbances of the turbulent flow. For small enough soap film thickness, the overall bubble density can be matched to that of air, by inflating the bubble with Helium. To this end, before each experiment, the bubble generator is carefully set up in order to adjust the thickness of the soap film. This procedure allows a precise control of the apparent density of the bubbles with respect to the fluid density (depending on the ambient temperature). Note that Helium-filling bubbles has also the additional benefit to increase the contrast of acoustic impedance between air and bubbles thus increasing the scattered amplitude.

Statistics for bubble radius have been obtained with the help of a video camera. It has been found that radius has a monodispersed distribution (1 mm ± 6%). This ensures that limitations due to bubble size will be at a constant scale. Production frequency has to be low enough to ensure that most of the time a single bubble is detected in the measurement volume. In practice, injection rates of about five bubbles/s gave reproducible results. Being injected upstream from the nozzle, only a small fraction of the injected bubbles will effectively reach the acoustic measurement volume. Besides, as we reject particles whose travel time is below some threshold value, still a smaller fraction, depending on the downstream position of the acoustic measurement volume, will be effectively retained for computation of the flow statistics. Actually, the overall fraction lies between 8.5% at $x = 1.3$ m and 6% at $x = 2.5$ m.

3 Signal processing

3.1 Channels separation

Figure 4 shows the power spectrum, estimated with the Welch averaged periodogram method, of a typical signal recorded on one of the receivers (during which around ten bubbles went through the measurement volume). One observes two sharp high-amplitude spikes exactly at the incoming frequencies. They correspond to direct propagation between emitter and receiver, as well as echoes. Beside each spike, at lower frequencies, stands a broader-band bump which corresponds to Doppler frequencies. To be able to obtain the two velocities, spikes have to be filtered out, and channels must be separated. Filtering out spikes removes a small part of the Doppler frequencies because of overlapping. This enforces a limitation on the smallest velocity that can be extracted (of order 0.5 m s^{-1}). Two notch filters are applied to remove the spikes, then a demodulation followed by a low-pass filtering allow the separation of the two scattered signals. We stress the fact that demodulation is performed by multiplication with a complex exponential (not a real cosine), yielding an analytic signal. The same operation is applied to the two signals recorded on the two receivers, leading to four different frequency-modulated signals, which will be denoted hereafter by s (s_i... s_l).

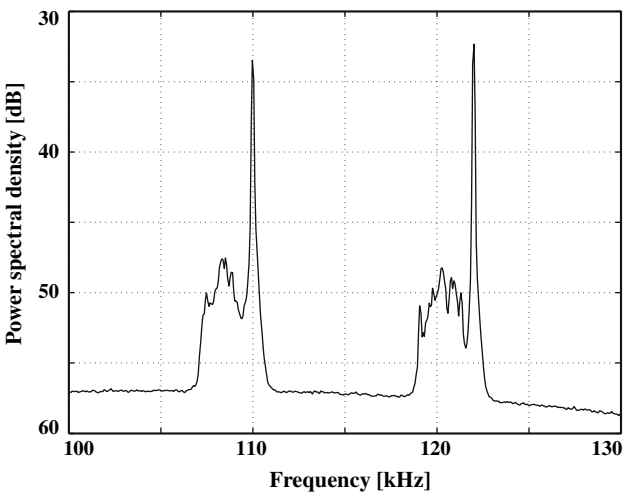

Fig. 4 Average power spectral density of the signal recorded by one of the receivers. The two sharp spectral lines are at the emitter frequencies (110 and 122 kHz), and correspond to waves propagating straight between two transducers (stray sound)

3.2 Time detection of tracers

The real part of one of the *s* signals is plotted in Fig. 5. We observe that the signal amplitude (computed as the complex magnitude) is very close to the enveloppe of the real part, confirming the analytical property of the signal. When a bubble is passing through the measurement volume, the signal amplitude rises. When no bubble is present, amplitude is not strictly zero. This remaining amplitude is due to sound scattering by the vorticity field (see Poulain et al. 2004). It will be considered as noise here.

A complex amplitude pattern, related to near field effects, is expected in the measurement volume. The scattered pressure signals recorded in the present experiment indeed exhibit significant amplitude modulations, as depicted in Fig. 5.

For a circular piston transducer the transition between the near field and the far field region occurs (on the axis) at a distance D_f from the transducer given by $D_f = L^2/4\lambda$ (where L is the transducer diameter and λ the acoustic wavelength). In the present study $L = 24$ cm, and $\lambda \simeq 3$ mm giving $D_f \simeq 5$ m. Nevertheless, Lagrangian velocities are obtained from the phase information of the scattered signals and thus are very weakly affected by near field effects as we do not rely on the amplitude information. We have checked that this was the case in our experimental configuration, by performing Doppler shift measurements on moving objects with a known velocity (for example an oscillating pendulum).

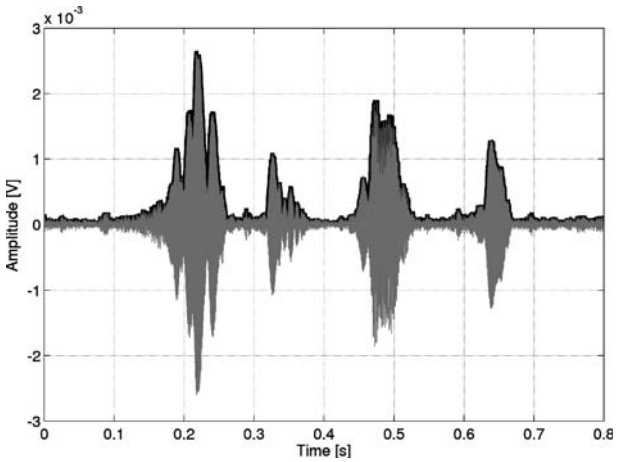

Fig. 5 Sample time record of the real part (*grey line*) and amplitude (*black line*) of the separated acoustic signal (*s*) recorded on one receiver, after a band pass filtering around one of the incident frequencies. The passage of four different bubbles inside the measurement volume is clearly identified by four bursts of the scattered acoustic intensity

Automatic detection of bubbles is achieved by a thresholding operation. Time intervals are determined by the following algorithm:

- Low-pass filtering of the signal amplitude (~4,000 Hz);
- Computation of the median of the former, as an estimation of noise level;
- Selection of time intervals where filtered amplitude is above twice the noise level;
- Rejection of intervals shorter than ten samples;
- Merging of intervals separated by no more than 5.3 ms (350 samples);
- Rejection of intervals shorter than 30 ms (2,000 samples).

This operation is applied independently on each of the *s* signals. For the velocity vector to be computed, the bubble should be detected at least on three signals simultaneously. Another selection procedure is thus applied to keep only intervals that have a common part on the four channels.

3.3 Signal to noise ratio maximisation

As explained before, the signal of interest is the wave scattered by the bubble. Noises include

(1) wave propagating straight between emitter and receiver and echoes;
(2) acoustic scattering by the vorticity fluctuations;
(3) overall electronic noise;
(4) turbulent acoustical noise.

In practice, (3) and (4) are of little concern. Acoustical amplitude can be made sufficiently large so that noise (3) is negligible. Noise (4) has only frequencies below 10 kHz, which is far from the band of study (100–150 kHz).

Once noise (3) has been overcome, increasing emitting power does not improve SNR, because signal and remaining noises (1) and (2) are all proportional to the incoming sound amplitude. So far no way has been found to reduce the noise (1).

Reducing the noise (2) can be achieved by adjustement of the scattering angles and of the working frequency. When frequency increases, the vorticity-scattered amplitude decreases (see Poulain 2004). Similarly, for a right scattering angle $\theta = \pi/2$, scattered amplitude is zero. Experiments have shown that bubble scattering cross section does not drop in the accessible frequency range, so that increasing the frequency increases the SNR. Above 130 kHz, sound absorption raises significantly, making noise (3) more and more important. As a consequence, time intervals

detected shorten (because beginning and end of segments are hidden by noise).

The final setup ($\theta = 128°$, frequencies between 110 and 130 kHz) is the result of a compromise between the following constraints:

- Longest measurement volume (largest θ)
- Lowest noise on the transverse components (smallest θ)
- Lowest vorticity scattering amplitude (highest frequency, θ near $\pi/2$)
- Lowest sound absorption (smallest θ, lowest frequency).

One can appreciate a typical SNR in Fig. 5.

3.4 Extracting velocity from acoustic signal

Two representations (either spectral- or time-) of the recorded signals have been used so far. None can give access to the bubble velocity, because it depends both on time and frequency. Determination of the velocity relies on an estimation of the instantaneous frequency. Cohen class energetic estimators are classical tools for this purpose. We chose the Choï–Williams distribution, for its moment-preserving property (Flandrin 1999). For a complex-valued analytic signal $x(t)$, its Choï–Williams distribution C_x is defined by:

$$\forall t, v \quad C_x(t,v) \widehat{=} \int_{-\infty}^{\infty}\int_{-\infty}^{\infty} \frac{\delta}{|\tau|} \mathrm{e}^{-2\delta^2(s-t)^2/\tau^2} x\left(s+\frac{\tau}{2}\right) x^*\left(s-\frac{\tau}{2}\right) \mathrm{e}^{-2\mathrm{i}\pi\nu\tau} \mathrm{d}s\mathrm{d}\tau \tag{3}$$

δ is a parameter. We used $\delta = 1$.

A sample result is shown in Fig. 6. Frequency is along the vertical axis, time along the horizontal axis. Grayscale levels quantify the energy level. Two crooked lines are visible, they correspond to two distinct bubbles. Following the maximum-energy line gives an idea of how velocity evolves along time, to a constant multiplicative factor (Eq. 1).

Automatic processing is based on this transformation. Hypothesis is made that each separated signal s have the form $x(t) = a(t)\exp(2\mathrm{i}\pi\ \varphi(t))$, where a and φ are two real functions. We also assume that φ is monotonic, so that $x(t)$ is analytic. The instantaneous frequency f of x is defined by the time derivative of φ. In terms of the time-frequency transformation, f can be expressed as:

$$\forall t, \quad f(t) = \frac{\int_{-\infty}^{\infty} \nu C_x(t,\nu)\mathrm{d}\nu}{\int_{-\infty}^{\infty} C_x(t,\nu)\mathrm{d}\nu}.$$

This formula cannot be directly applied to experimental signals, because of noise, that strongly biases the result. First, in the above expression the integration must be performed up to some maximum Doppler shift frequency, in order to limit the noise contribution. In practice, this high frequency limitation, imposed on the four projection signals v_i, v_j, v_k, v_l, fixes a limit on the maximum accessible longitudinal velocity u (of order 3.5 standard deviations above the mean value for all distances). The estimation of $f(t)$ is actually done in two steps. For a given time, frequency corresponding to the maximum of energy is determined. Instantaneous frequency is then computed according to the above formula, restricted to a small frequency interval around the maximum. Obviously, only a discrete version of formula 3 can be computed, in which 512 frequency bins were used. Due to the large sampling frequency, useful Doppler signals span around 30 bins only. f is computed on a 7-bin wide interval.

This velocity extraction is applied to each s signal, on the selected intervals. Coordinate transformation yields lots of small (2,000–8,000 points) velocity signals which will be called ''velocity segments'' in the following. No time continuity exists between velocity segments, they all correspond to different bubbles. Such a procedure leads to a large set of independent realizations of Lagrangian velocities. The j-th point (time) of the i-th segment (realization) will be denoted by $\mathbf{v}_i(j)$.

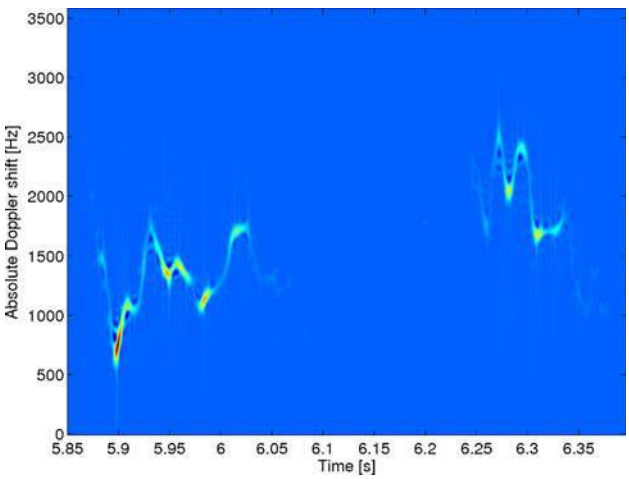

Fig. 6 Time-frequency representation of the scattered acoustic intensity computed from the demodulated signal recorded on one of the two receivers. Two bubble signals are clearly visible. The horizontal axis displays the time dependence, the vertical axis indicates the doppler shift relative to the incident frequency and the instantaneous acoustic intensity is coded by the color

4 Results

4.1 Data set

The experimental setup was designed with correlation measurements in mind. Therefore, the velocity of each bubble had to be measured for as long as possible (see 2.2). This lead us to use a jet with a small nozzle diameter compared to the transducers diameter. For technical reasons, the mean velocity could not be very high, leading to a moderately high Reynolds number ($R_\lambda \simeq 320$). Series of recordings were made at four distances ($D = x/d$) from the nozzle. Every measurement corresponds to the same Reynolds number, as it is constant along the jet, but to different integral length scales (Pope 2000; Wygnanski and Fiedler 1969; Tennekes and Lumley 1992). The measurement volume was centered on the jet axis, to preserve cylindrical symmetry as much as possible.

Table 3 lists some parameters (time, scale and velocity) for all the measurements. The number of velocity segments exceeds 1,000 for all measurements, ensuring good statistical convergence. Measurement volume length is several times larger than the Eulerian integral length scale (L_s/L_E), and the ratio of the maximal time-of-flight to the expected Lagrangian integral time scale (T_s/T_L) is everywhere above one (see 2). This estimation is in good agreement with the experimental ratio $\langle T_s \rangle / T_L$, which involves the mean time-of-flight and the measured Lagrangian integral time scale. Values of $\langle T_s \rangle / T_L$ decreases with increasing nozzle distance, as expected.

4.2 Probability density function

Like most free shear flows, the axisymetric jet flow is not spatially homogeneous. In particular, the mean streamwise velocity evolves continuously in both the downstream and the transverse directions. As we shall see later, the consequence of such lack of spatial homogeneity on distances comparable to the integral lengthscale is responsible for a lack of stationarity of the Lagrangian velocity trajectories. Considering that particles are injected at the same downstream position, from the view point of ensemble average (over all Lagrangian trajectories), the statistics (mean and standard deviation) of the Lagrangian velocity will depend on the time elapsed between the injection and the current time of the measurement. However, for downstream distances larger than 40 diameters, Eulerian statistics of the axisymetric jet flow are known to follow the so-called self-similarity property. For round jets, this self-similarity property manifests as a linear evolution of the inverse of the mean and standard deviation of the velocity components with respect to the downstream position: $u \propto (x - x_0)^{-1}$ (where x_0 is some virtual origin, usually found close to four times the nozzle diameter (Pope 2000).

Figure 7 shows that the same property is also true for Lagrangian velocity statistics, obtained by averaging all data of the available velocity segments in each of the four downstream measurement positions. Clearly, self-similarity exists except for the farthest downstream position. This result suggests that the inhomogeneity effects are rather weak, and justify, a posteriori our choice of duration threshold we did for the first three positions.

Normalized probability density functions (PDF) for the longitudinal velocity component are presented in Fig. 8. No systematic differences in the shape of the PDF can be seen between the four curves, indicating that the variation of L_s/L_E does not break self-similarity. The same remark is true for transverse components (Fig. 9). All curves are Gaussian, but small departures exist (for deviations from the mean value larger than $\pm 2.5\sigma$). For the longitudinal component (Fig. 8), PDF edges are sub-Gaussian due to frequency limitations at both low and high Doppler shifts, of the velocity extraction algorithm (see sect. 4) and has no physical origin. For transverse components (Fig. 9), edges are over-Gaussian because of noise introduced by the velocity extraction algorithm. Previous studies by Mordant have also shown that the Lagrangian velocity probability density function in a Von-Kármán

Table 3 Velocity statistics for the four experiments. Distance D is taken between nozzle and center of measurement volume (in units of of nozzle diameter). N is the number of velocity segments, L_E and T_L the integral Eulerian lengthscale and Lagrangian timescale, respectively. The last four columns display Lagrangian velocity statistics

D	N	L_E (cm)	T_L (ms)	$\frac{L_s}{L_E}$	$\frac{\langle T_s \rangle}{T_L}$	$\frac{T_s}{T_L}$	$\langle U_L \rangle [\mathrm{m\,s^{-1}}]$	$\frac{u^L_{rms}}{\langle U_L \rangle}$	$\frac{v^L_{rms}}{\langle U_L \rangle}$	$\frac{w^L_{rms}}{\langle U_L \rangle}$
58	3,552	6.2	35	8.1	1.48	2.6	4.25	0.29	0.23	0.23
80	9,584	8.8	60	5.7	1.22	1.8	3.10	0.27	0.23	0.23
93	7,444	10.3	80	5.0	1.20	1.6	2.59	0.27	0.24	0.25
111	1,358	12.3	120	4.2	1.02	1.3	2.09	0.30	0.26	0.26

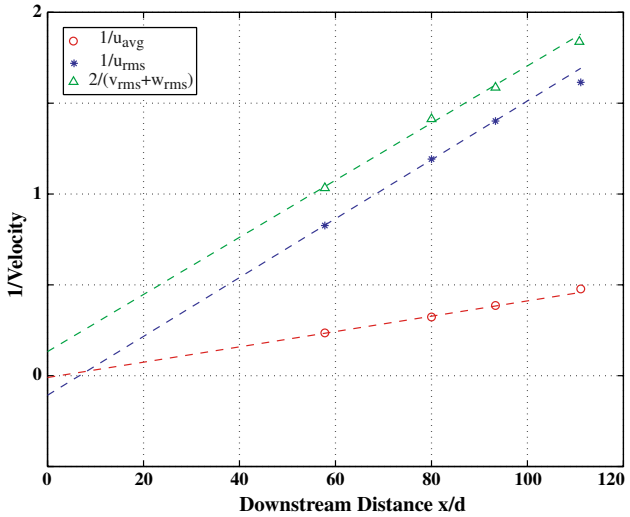

Fig. 7 Evolutions of the mean and standard values of the Lagrangian velocity components, with the downstream position

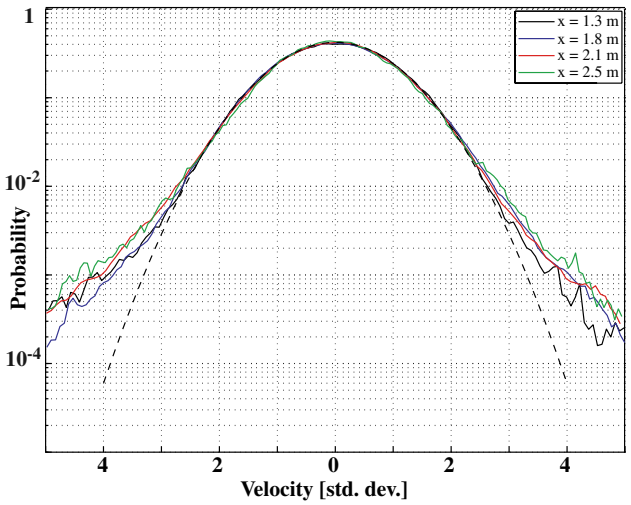

Fig. 9 Same as Fig. 8: PDF of the normalized transverse velocity (zero mean and unity variance). The corresponding Gaussian curve is plotted in *dashed line*

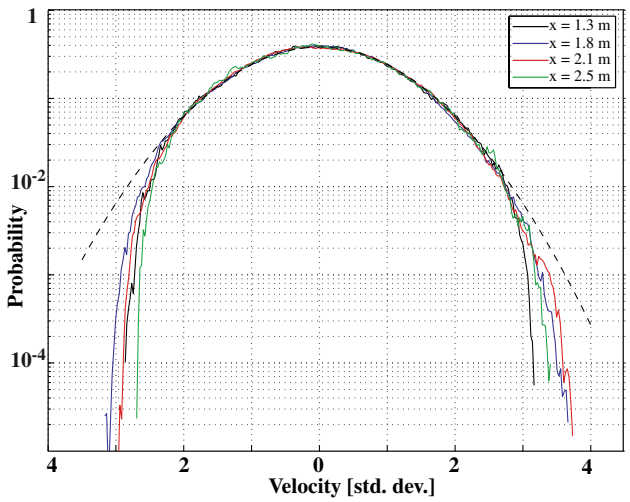

Fig. 8 PDF of the n ormalized longitudinal velocity (zero mean and unity variance) at the four investigated downstream positions. The corresponding Gaussian curve is plotted in *dashed line*

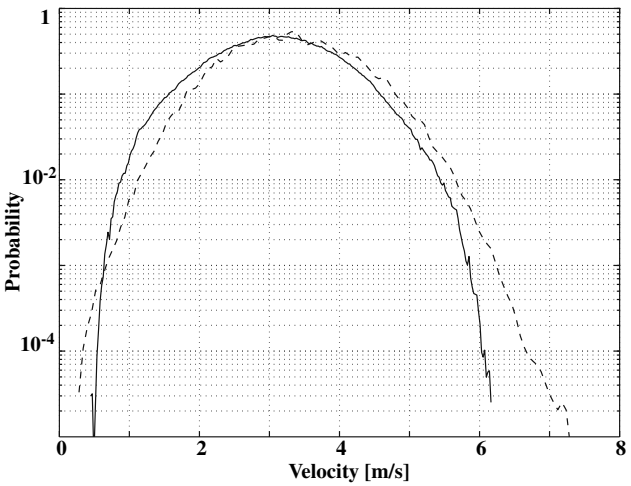

Fig. 10 Comparison of the Lagrangian (*solid line*) and Eulerian (*dashed line*) velocity PDF, recorded at the downstream position, 80 diameters from the nozzle

flow has a Gaussian shape, despite its well known large-scale flow inhomogeneity (mean and fluctuations).

Figure 10 shows the comparison of the Lagrangian PDF ($P(u)$) with the corresponding Eulerian one (the hot-wire was located near the center of the Lagrangian measurement zone). A reasonable agreement is found. A slightly higher mean velocity is found in the Eulerian case (5% higher), which can be explained by the fact that the hot-wire was located on the jet axis, where the mean velocity reaches its maximum value.

Figure 11 shows isocontours of the joint PDF $P(u,v)$ of longitudinal u and transverse v Lagrangian velocity. A slightly elliptical shape is visible, indicating that no large-scale isotropy exists (horizontal and vertical coordinates are identical). Standard deviation of the longitudinal component is higher than the corresponding one for the transverse component, by a factor ranging from 1.1 to 1.25, depending on the position along the jet (farthest and nearest from the nozzle, respectively). A similar behaviour exists for Eulerian velocity components, with a ratio close to 1.29 (see Wygnanski and Fiedler 1969; Pope 2000). Actually, the difference between the two ratio is compatible with the fact that due to larger noise contamination, the standard deviation of the Lagrangian transverse compo-

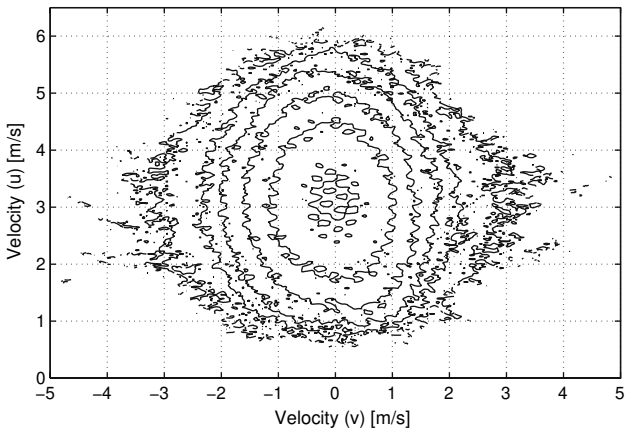

Fig. 11 Isocontours of joint Lagrangian velocity PDF $P(u,v)$ at the downst ream position $x/d = 80$. Contour values, from the center outward, are 3.16 10^{-4}, 10^{-4}, 3.16 10^{-5}, 10^{-5}, 3.16 10^{-6}, 3.16 10^{-7}

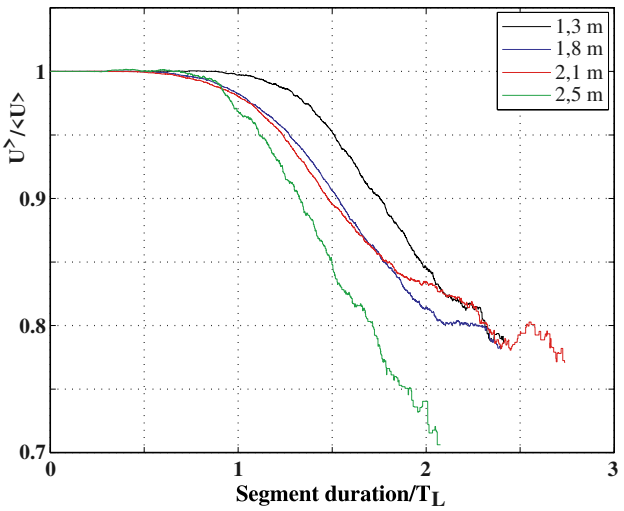

Fig. 12 Mean longitudinal velocity computed over segments longer than a specified duration at the four downstream measurement positions x/d = 58, 80, 93, 111

nents could be slightly over-estimated. Moreover, in our case the evolution of the ratio $u^{\mathrm{L}}_{\mathrm{rms}}/v^{L}_{rms}$ (see columns 3–9 of Table 3) can also be partly explained by the decreasing of the ratio between the lateral size of the measurement volume and the local transverse integral length scale L_{E}, as noticed in sect. 2.4.

4.3 Statistical estimation of correlation

Measurements by laser Doppler anemometry are biased towards lower velocities because slowest particles spend more time in the measurement volume. The same phenomenon exists in the present Lagrangian measurements performed in a non-zero mean velocity flow. Average velocity and standard deviation considered on segments longer than a specified duration k (respectively noted $\mathbf{v}^{>}(k)$ and $\boldsymbol{\sigma}^{>}(k)$) are computed with the help of the following formula, where L_i is the length of segment i (j standing for the current time on each bubble trajectory):

$$\forall k = 1..\max_i L_i, \quad \mathbf{v}^{>}(k) \widehat{=} \frac{\sum_{i|L_i>k} \sum_{j=1}^{L_i} \mathbf{v}_i(j)}{\sum_{i|L_i>k} L_i}$$

$$\forall k, l, \quad (\boldsymbol{\sigma}^{>}(k))_l \widehat{=} \sqrt{\frac{\sum_{i|L_i>k} \sum_{j=1}^{L_i} (\mathbf{v}_i(j))_l^2}{\sum_{i|L_i>k} L_i} - (\mathbf{v}^{>}(k))_l^2}$$

$(\boldsymbol{\sigma}^{>})_l$ is the l-th component of vector $(\boldsymbol{\sigma}^{>})$. Figure 12 shows the curves obtained for the longitudinal component $\mathbf{v}^{>}(k)$, at the four locations. Every curve shows a plateau which falls off at long times ($\boldsymbol{\sigma}^{>}(k)$ exhibits similar shapes, not shown here). This indicates that a bias exists, stronger for the longest segments, that must be corrected for. Especially, estimation of autocorrelation is strongly influenced, because values for the longest time lags can only be computed with the longest segments, that is, the biased points.

If no bias in the signals were present, the classical formula for correlation estimation could be used (Eq. 4), and the global mean $\langle \mathbf{v} \rangle$ and standard deviation $\boldsymbol{\sigma}$ would be used.

$$\forall l \forall k, \quad R_{ll}(k) \widehat{=} \frac{1}{(\boldsymbol{\sigma})_l^2 \sum_{i|Li>k} L_i - k} \sum_{i|L_i>k} \sum_{j=1}^{L_i-k} \left[(\mathbf{v}_i(j))_l - \langle \mathbf{v} \rangle_l\right] \left[(\mathbf{v}_i(j+k))_l - \langle \mathbf{v} \rangle_l\right]. \tag{4}$$

In order to compensate for the bias, values for mean and standard deviation have to be different for each time lag. Computation of correlation value for time lag k involves only segments longer than k. As suggested in Yeung (2002), we introduce in the formula the previously defined mean $\mathbf{v}^{>}(k)$ and standard deviation $\boldsymbol{\sigma}^{>}(k)$ (equation 5).

$$\forall k, \quad R_{ll}(k) \widehat{=} \frac{1}{\sum_{i|L_i>k} L_i - k} \sum_{i|L_i>k} \sum_{j=1}^{L_i-k} \frac{(\mathbf{v}_i(j))_l - (\mathbf{v}^{>}(k))_l}{(\boldsymbol{\sigma}^{>}(k))_l} \frac{(\mathbf{v}_i(j+k))_l - (\mathbf{v}^{>}(k))_l}{(\boldsymbol{\sigma}^{>}(k))_l}. \tag{5}$$

In expression 5, $\mathbf{v}^{>}(k)$ is the output of both an ensemble average over all velocity segments i (considered at the same given time lag j from the origin) and a time

average (cumulative average up to time lag k). Should every particle enters in the measurement volume at a fixed and known location (initial position at some time t_0), then this averaging would give the true mean value after a given delay t–t_0 (within statistical uncertainty). Then it would allow for an exact compensation of the bias due to the decreasing of the mean velocity along the jet axis. Unfortunately, our measurement set-up does not provide such initial particle position. Thus, the ensemble average is partly biased even though, actually, the particles are expected to enter in the measurement volume at more or less the same downstream position. From this viewpoint, the time averaging tends to generate an ersatz of mean initial entering position over all particle trajectories. Figure 12 shows the behaviour of the streamwise component $\mathbf{v}^{>}(k)$ (normalized by its value at the initial measurement time t_0 when the particle enters the measurement volume) against the velocity segment duration (normalized by the local Eulerian integral time-scale). We observed that the average value $\mathbf{v}^{>}(k)$ is constant (within 5%) over 1.5 times the integral time-scale at the nozzle nearest location and only 1 integral time-scale at the farthest one. The departure observed for the largest downstream distance is probably correlative of the departure from self-similarity noticed in the previous section (see Fig. 7). In the latter case, the loss of uniformity of the mean velocity mainly reveals the non uniform distribution of the particles across the measurement volume. On the contrary, the curve corresponding to the nearest position, is dominated by the transverse inhomogeneity of the velocity profile. Probably, the effect of these two inhomogeneities are of the same order for the two intermediate positions which can explain why the two corresponding curves are almost the same.

Actually, expression 5 has been used for computing the autocorrelations presented in the following, for both three components. It is worth noticing that, as the bias is mainly due to the downstream evolution of the mean streamwise velocity, it should less affect transverse components (which have a constant zero mean). Accordingly, for transverse components no significant difference between the two correlation estimations are observed.

4.4 Correlations

Autocorrelation of Lagrangian velocity components as well as Eulerian longitudinal one are presented in Figs. 13 and 14 (corresponding to the measurements performed at 80 diameters from the nozzle). The two curves for Lagrangian transverse components are almost identical, in accordance with the axial symmetry of the flow. The longitudinal component exhibits a slightly longer time scale.

We denote in the following the longitudinal and transverse Lagrangian integral time scales by $T_{\mathrm{L}}^{\mathrm{l}}$ and $T_{\mathrm{L}}^{\mathrm{t}}$, respectively. These values are computed by fitting an exponential curve on the autocorrelation. It is interesting to note that the longitudinal autocorrelation curve (black solid line in Fig. 13), when normalized by its integral time-scale T_{L}^{ℓ} has precisely the same shape than those obtained by Mordant et al. (2001), Sato and Yamamoto (1987) and Shlien and Corrsin (1974) in different flow situations and for various Reynolds numbers ($65 \leq R_\lambda \leq 740$). It is somewhat remarkable that such Lagrangian autocorrelation has a so constant shape.

Corresponding values for Eulerian components are denoted by $T_{\mathrm{E}}^{\mathrm{l}}$ and $T_{\mathrm{E}}^{\mathrm{t}}$. Only $T_{\mathrm{E}}^{\mathrm{l}}$ can be readily obtained from measurements: $T_{\mathrm{E}}^{\mathrm{l}} \widehat{=} L_{\mathrm{E}}^{\mathrm{l}}/\sigma_{\mathrm{E}}^{\mathrm{l}}$, where $L_{\mathrm{E}}^{\mathrm{l}}$ is the Eulerian integral length scale (obtained from the autocorrelation and Taylor hypothesis), and σ_E^{l} is the standard deviation of the longitudinal Eulerian velocity. As no measurement of transverse Eulerian velocity has been performed, T_E^{t} is estimated from the longitudinal value, assuming that $L_{\mathrm{E}}^{\mathrm{l}}/L_{\mathrm{E}}^{\mathrm{t}} \simeq 2.3$ and $\sigma_{\mathrm{E}}^{\mathrm{l}}/\sigma_{\mathrm{E}}^{\mathrm{t}} \simeq 1.2$ (as reported in Wygnanski and Fiedler 1969). All these values are listed in Table 4. One note that transverse integral time scales are smaller than for longitudinal component. In the Eulerian case, the ratio (seventh column of Table 4) exhibits no dependence on the distance x from the nozzle, in accordance with

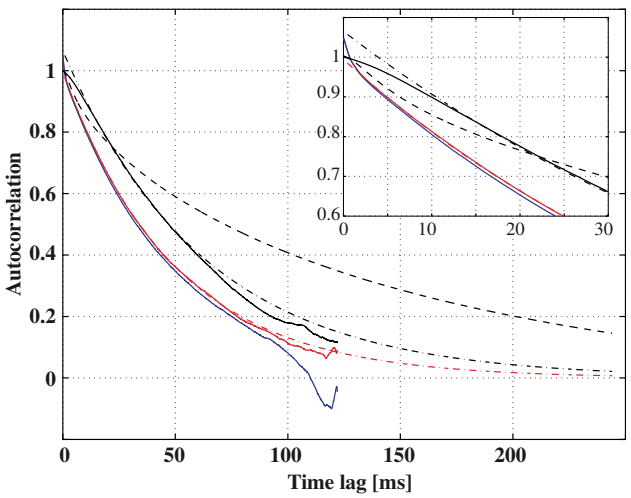

Fig. 13 Lin-lin plots of Lagrangian velocity autocorrelation (*solid lines*) for longitudinal (*black*) and transverse components (*red* and *blue*), measured at the downsteam position $x/d = 80$. Eulerian streamwise velocity autocorrelation (*dashed line*). An exponential fit has been superimposed to Lagrangian correlations (*dot-dashed line*). *Inset* zoom on the smaller time-lags

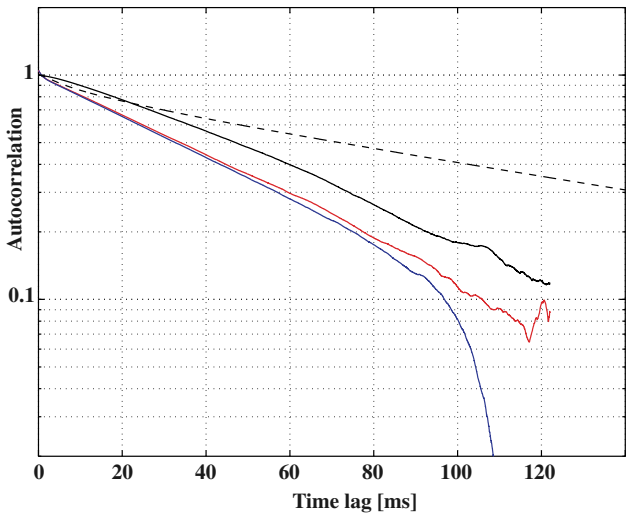

Fig. 14 Semilog plots of Lagrangian velocity autocorrelation (*solid lines*) for longitudinal (*black*) and transverse components (*red* and *blue*), measured at the downsteam position x/d = 80. Eulerian streamwise velocity autocorrelation (*dashed line*)

Table 4 Eulerian and Lagrangian time scales in milliseconds. $T_{\mathrm{L}}^{\mathrm{l}}$, $T_{\mathrm{L}}^{\mathrm{t}}$ and $T_{\mathrm{E}}^{\mathrm{l}}$ measured. $T_{\mathrm{E}}^{\mathrm{t}}$ computed from $T_{\mathrm{E}}^{\mathrm{l}}$ (see text)

D	$T_{\mathrm{L}}^{\mathrm{l}}$	$T_{\mathrm{L}}^{\mathrm{t}}$	$\frac{T_L^l}{T_L^t}$	$T_{\mathrm{E}}^{\mathrm{l}}$	$T_{\mathrm{E}}^{\mathrm{t}}$	$\frac{T_E^l}{T_E^t}$	$\frac{T_E^l}{T_L^l}$	$\frac{T_E^t}{T_L^t}$
58	35	26	1.35	48	25	1.92	1.37	0.98
80	62	49	1.27	98	51	1.92	1.58	1.04
93	79	59	1.34	129	69	1.92	1.63	1.16
111	117	75	1.56	205	98	1.92	1.75	1.30

the previous hypotheses. In the Lagrangian case, we observed that this ratio (fourth column of Table 4) is also constant with the downstream distance x, except for the farthest position where data are less reliable (as previously noticed). Compared to the Eulerian value (estimated to 1.92) the Lagrangian ratio is smaller and experimentally found close to 1.31 ± 5%. Such values could suggest that large scale anisotropy would affect more the spatial shape of the large coherent structures than their own life time. In addition, the constancy of the ratios $\frac{T_{\mathrm{L}}^{\ell}}{T_{\mathrm{L}}^{\mathrm{t}}}$ and $\frac{T_{\mathrm{E}}^{\ell}}{T_{\mathrm{E}}^{\mathrm{t}}}$ reduces the analysis of the Eulerian and Lagrangian large time-scales to the only comparison of the longitudinal timescales T_{L}^{ℓ} and T_{E}^{ℓ}. Of course, these two timescales scale with the downstream distance as D^2 but with different prefactors. Our measurements show that the ratio T_{E}^{ℓ} / T_{L}^{ℓ} increases very weakly with D (namely, 1.4, 1.6, 1.65 and 1.75 respectively at 50, 80, 93 and 111 nozzle diameters).

Since, the Lagrangian time T_{L} can be considered as a rough measure of the real eddy life-time whereas T_{E} is related to the turnover time (mainly used for phenomenological analysis), our results show that the life time is slighty shorter than the usual turnover time.

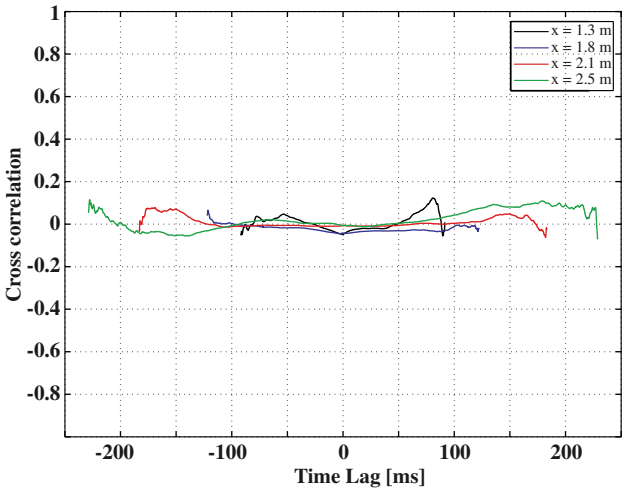

Fig. 15 Cross correlation of transverse components v and w of Lagrangian velocities,s measured at the four downstream measurement positions x/d = 58, 80, 93, 111

Despite the large scale inhomogeneity, our values are comparable to the well accepted ones, in particular, they are slightly greater than the value 1/0.78 = 1.28 proposed in Yeung (2001).

A first phenomenological approach leads to $T_{\mathrm{L}} \simeq T_{\mathrm{E}}$ (Corrsin 1963). A larger Eulerian time scale with respect to the Lagrangian one can be explained by the so-called sweeping effect. In fact, the random advection of the internal scales by the energy-containing scale leads to broadening of the Eulerian autocorrelation in comparison with the Lagrangian one (Kraichnan 1964). Such a reason could explain a larger value of the Eulerian integral scale with respect to the Lagrangian one.

Cross correlations of transverse Lagrangian components (v,w) are shown in Fig. 15. All curves are very close to zero (noise floor is about 0.05), showing that no correlation exists between the lagrangian velocity components, despite the large scale anistropy of the jet flow in the measurement volume (it is also true for the cross-correlations u–v and u–w, not shown). It is worth noticing here that in the Eulerian frame, velocity components are far from being decorrelated (the correlation coefficient ρ_{uv} reaches values as high as 0.4, see e.g. Pope 2000). This supports one-dimensional modeling of fluid particle large-scale motion. Besides, such decorrelation between the components of the Lagrangian velocity in three orthogonal directions is an a posteriori validation of the geometry of the present measurement setup. Indeed, taking for granted that Lagrangian velocity components are mutually decorrelated (also reported by Mordant et al. (2001)), any relative misalignment of the four transducers collecting the velocity projections (i, j, k, l) would necessarily

result in residual cross-correlation between orthogonal components.

5 Conclusions

Lagrangian measurements in a free turbulent air jet were performed using acoustical Doppler effect. This method is adapted to collecting large data sets without tremendous memory requirement, contrary to visualisation methods. A true three-dimensional volume measurement is achieved, as the setup does not suffer from depth of field effect. Simultaneous Eulerian measurements were performed, which to our knowledge has never been reported before. A single tracer at a time can be detected, with the time- and space-dynamics of the measurements comprising a large part of the inertial scales, comparable to previously obtained results (Mordant et al. 2001).

As in most of real turbulent flows, jets are characterized by significant departures from homogeneity in both spanwise and streamwise directions. Longitudinal inhomogeneity has been properly compensated for the velocity correlation estimations (first and second order stationarization). As far as spanwise inhomogeneity is concerned, it will be necessary to condition the velocity statistics on the transverse particule positions (at least the initial ones). A main advantage of the present acoustic Doppler method (providing a direct access to particles velocity, without resorting to, usually noisy, differentiation procedures) is that the full particles positions (at all times) will only require the determination, at some known initial time, of the initial particle position in a single transverse section of the flow (instead of a full volume).

The present study focused on the correlation properties of the flow. The long-standing issue of the ratio of Eulerian and Lagrangian time scales has been partially answered experimentally. The fact that $T_{\mathrm{E}}^{1} > T_{\mathrm{L}}^{1}$ is probably a consequence of the fact that Eulerian statistics are affected by sweeping, whereas Lagrangian ones are not. This result holds for distances in the jet ranging from 60 nozzle diameters up to 110 nozzle diameters. Preliminary analysis of the correlation curves (not reported here) seems to indicate that the time microscales differ between Lagrangian and Eulerian field, indicating that the inertial range is not identical (shorter for the Lagrangian field). Further experimental confirmation needs a detailed study of the influence of the finite viscous response time of the particles. A better comprehension of the viscous effects is also mandatory for the statistical analysis of Lagrangian velocity time increments and will be reported elsewhere. Large-scale statistics do not depend significantly on Reynolds number, whereas small-scale ones do. Thus a devoted study of inertial and dissipative scales requires new measurements, for different Reynolds numbers.

Acknowledgments This work is fully supported by the French Ministère de la Recherche and by the Université Joseph Fourier (PPF plateforme expérimentale de spectroscopie acoustique multi-échelles). We are fully indebted to both reviewers for pointing out in their reports, the importance of the flow inhomegeneity in the context of Lagrangian measurements. We thank Michel Lebey for kindly lending us their bubble machine. We wish to acknowledge fruitful discussions with Jean-Francois Pinton and Laurent Chevillard. We also thank Jean-Paul Barbier-Neyret and Joseph Virone for their valuable technical help.

References

Bec J, Biferale L, Boffetta G, Celani A, Cencini M, Lanotte A, Musacchio S, Toschi F (2006) Acceleration statistics of heavy particles in turbulence. J Fluid Mech 550:349–358

Corrsin S (1963) Estimates of the relations between Eulerian and Lagrangian scales in large Reynolds number turbulence. J Atmos Sci 20(2):115–119

Flandrin P (1999) Time–frequency/Time-scale analysis. Academic, London

Kraichnan RH (1964) Relation between lagrangian and eulerian correlation times of a turbulent velocity field. Phys Fluids 7(1):142–143

Maxey MR, Riley JJ (1983) Equation of motion for a small rigid sphere in a nonuniform flow. Phys Fluids 26(4):883–889

Monin AS, Yaglom AM (1975) Statistical fluid mechanics. MIT press, Paris

Mordant N, Metz P, Michel O, Pinton JF (2001) Measurement of lagrangian velocity in fully developed turbulence. Phys Rev Lett 87(21):214–501

Ott S, Mann J (2000) An experimental investigation of the relative diffusion of particle pairs in three-dimensional turbulent flow. J Fluid Mech 422:207–223

Pope SB (2000) Turbulent flows. Cambridge University Press, Cambridge

Poulain C, Mazellier N, Gervais P, Gagne Y, Baudet C (2004) Spectral vorticity and lagrangian velocity measurements in turbulent jets. Flow Turbul Combust 72:245–271

Sato Y, Yamamoto K (1987) Lagrangian measurement of fluid-particle motion in an isotropic turbulent field. J Fluid Mech 175:183–199

Shlien DJ, Corrsin S (1974) A measurement of lagrangian velocity autocorrelation in approximately isotropic turbulence. J Fluid Mech 62(2):255–271

Tennekes H, Lumley JL (1992) A first course in turbulence. MIT press, Paris

Virant M, Dracos T (1997) 3D PTV and its application on lagrangian motion. Meas Sci Technol 8:1539–1552

Voth GA, la Porta A, Crawford AM, Alexander J, Bodenschatz E (2002) Measurement of particle accelerations in fully developed turbulence. J Fluid Mech 469:121–160

Wygnanski I, Fiedler H (1969) Some measurements in the self-preserving jet. J Fluid Mech 38(3):577–612

Yeung PK (2001) Lagrangian characteristics of turbulence and scalar transport in direct numerical simulations. J Fluid Mech 428:241–274

Yeung PK (2002) Lagrangian investigations of turbulence. Ann Rev Fluid Mech 34:115–142